

Water-induced Diamond Formation at Earth's Core-Mantle Boundary

Byeongkwan Ko^{1*}, Stella Chariton², Vitali Prakapenka², Bin Chen³, Edward J. Garnero¹,
Mingming Li¹, Sang-Heon Shim¹

¹School of Earth and Space Exploration, Arizona State University, Tempe, AZ, USA

²Center for Advanced Radiation Sources, University of Chicago, Chicago, IL, USA

³Hawaii Institute of Geophysics and Planetology, University of Hawaii at Manoa, Honolulu, HI,
USA

*Now at Department of Earth and Environmental Sciences, Michigan State University, East
Lansing, MI, USA

Corresponding author: Byeongkwan Ko (kobyong@msu.edu)

Key Points

- Water reacts with iron-carbon alloy to form diamond at the P - T conditions expected for Earth's core-mantle boundary.
- Some of Earth's mantle carbon may come from the core through water-induced reactions at the core-mantle boundary.
- Diamonds formed at the core-mantle boundary may result in high seismic velocity structures in the region.

22

23 **Abstract**

24 The carbon and water cycles in the Earth's interior are linked to key planetary processes, such as
25 mantle melting, degassing, chemical differentiation, and advection. However, the role of water in
26 the carbon exchange between the mantle and core is not well known. Here, we show experimental
27 results of a reaction between Fe_3C and H_2O at pressures and temperatures of the deep mantle and
28 core-mantle boundary (CMB). The reaction produces diamond, FeO , and FeH_x , suggesting that
29 water can liberate carbon from the core in the form of diamond ("core carbon extraction") while
30 the core gains hydrogen, if subducted water reaches to the CMB. Therefore, Earth's deep water
31 and carbon cycles can be linked. The extracted core carbon can explain a significant amount of the
32 present-day mantle carbon. Also, if diamond can be collected by mantle flow in the region, it can
33 result in unusually high seismic-velocity structures.

34 **Plain Language Summary**

35 Carbon plays a vital role in geological processes occurring in the Earth's interior. While most
36 carbon on Earth exists in its core, whether or not the core carbon can be added to the mantle is
37 unclear due to the lack of knowledge of possible carbon transfer mechanism at the core-mantle
38 boundary (CMB). We conducted experiments by reproducing the extreme pressure and
39 temperature conditions of the CMB. Our experiments show that water can react with the metallic
40 iron core and liberate carbon as diamond, suggesting an important relationship between Earth's
41 water and carbon cycles on Earth. In addition, our result predicts possible existence of diamond in
42 some regions of the deepest mantle.

43 **1 Introduction**

44 Distribution of carbon in its interior provides important clues for understanding the chemical
45 evolution of the Earth. During the accretion processes, a vast majority of Earth's carbon could
46 have been added to the core because of carbon's siderophile nature (Dasgupta et al., 2013; Fischer
47 et al., 2020). The preferential partitioning of carbon into the metallic core predicts a very small

48 amount of residual carbon in the silicate mantle after core formation (1–5 ppm; Dasgupta et al.,
49 2013). However, the estimated carbon abundance in the present-day mantle is much greater
50 (~120 ppm for pyrolite; McDonough and Sun, 1995). It remains unclear how the mantle has
51 gained much more carbon (Dasgupta et al., 2013).

52 Several models for carbon replenishment to the mantle have been proposed to explain the present-
53 day mantle inventory of carbon. For example, the additional carbon might have been delivered
54 through a volatile-rich late veneer that occurred after core formation (Wänke, 1981). This model
55 has difficulties explaining the difference in carbon isotopic composition between CI chondritic
56 materials and the average mantle (Kerridge, 1985; Deines, 2002) and the superchondritic H/C ratio
57 of the bulk silicate Earth in present day (Hirschmann and Dasgupta, 2009). Alternatively, carbon
58 ingassing might have occurred after core formation. Carbon in an early atmosphere might have
59 dissolved into an early magma ocean and precipitated graphite, diamond, or carbide, increasing
60 the amount of the mantle carbon (Dasgupta et al., 2013). Also, some amount of carbon-bearing
61 metallic melts might have been trapped in the mantle if incomplete segregation of metallic liquid
62 from the mantle occurred during core formation (Dasgupta et al., 2013).

63 The core is the largest carbon reservoir within the Earth (McDonough, 2003), although estimates
64 of the amount of carbon in the core vary, e.g., between 0.09–4 wt% (McDonough, 2003; Dasgupta
65 and Walker, 2008; Wood et al., 2013; Dasgupta et al., 2013; Fischer et al., 2020). Therefore, core
66 carbon loss to the mantle through CMB chemical reactions after core formation could be a viable
67 source for the observed excess mantle carbon. Dasgupta et al. (2013) predicted that if deeply
68 subducted hydrous minerals break down and release water at the CMB, water may react with the
69 iron core. They further speculated that the reaction would form FeH_x and liberate carbon from the
70 iron core by forming CO , CO_2 , or FeCO_3 . This hypothesis suggests that Earth's carbon, hydrogen,
71 and water cycles may be linked at the CMB. Experiments have demonstrated the plausibility of
72 hydrous minerals in subducting slabs, such as AlOOH (Piet et al., 2020), FeOOH (Nishi et al.,
73 2017), phase H (Nishi et al., 2014), and hydrous SiO_2 (Lin et al., 2020; Nisr et al., 2020). Thus,
74 subduction processes can result in the transport and release of water in the deepest mantle, although
75 dehydration processes at the CMB could be more complicated than what has been observed in
76 experiments on simplified chemical systems.

77

78 H, O, and C are all light element candidates for the core (e.g., Hirose et al., 2013), which could
79 affect one another's solubility in the region. Experiments showed that $C_nH_{(2n+2)}$ paraffin reacts
80 with Fe and forms Fe_3C , which was then replaced by FeH_x + diamond at 64 GPa and 1,650 K
81 (Narygina et al., 2011) and up to 127 GPa and >2,100 K (Hirose et al., 2019). Hirose et al. (2019)
82 also showed that the same reaction occurs even with liquid Fe at 58–66 GPa and 3,220–3,710 K.
83 It thus appears that hydrogen's strong affinity to iron could lower the solubility of C in the core.
84 However, whether iron carbide directly react with water to liberate carbon at pressure and
85 temperature (P – T) conditions relevant to the CMB has never been tested by experiments. In order
86 to understand the possibility of carbon exchange between the core and the mantle induced by the
87 presence of water at the CMB, we conducted experiments on reactions between iron carbide
88 (Fe_3C) and water (H_2O) at 70–140 GPa and up to 4,050 K (thus bracketing the CMB pressure of
89 136 GPa) using in-situ X-ray diffraction (XRD) in laser-heated diamond anvil cells (LHDACs).
90 The experiments found formation of diamond from reaction between iron carbide and water,
91 opening up a possibility for the chemical exchange between the core and the mantle.

92 **2 Materials and Methods**

93 Fe_3C was synthesized at high pressures using the multi-anvil press at the University of Hawaii at
94 Manoa. The starting material was a mixture of Fe powder (99.9+% purity, Aldrich Chemical
95 Company) and graphite powder (99.9995% purity, Alfa Aesar Company) with an atomic ratio
96 Fe:C = 3:1. The mixture was loaded into a MgO capsule of an 18/12 multi-anvil cell assembly,
97 which was then compressed to 3 GPa and heated at 1,300 K for 8 hours to synthesize Fe_3C . The
98 Fe_3C sample was then analyzed by electron microprobe to confirm its purity and composition. The
99 synthesized Fe_3C was loaded as ~ 10 μm -thick foils in the symmetric-type LHDACs with 150 and
100 200 μm -sized culets using a micro-manipulator (Microsupport Axis Pro SS) at Arizona State
101 University (ASU). Distilled water was loaded as a pressure medium.

102 In-situ X-ray diffraction (XRD) experiments (Table 1) were conducted at sector 13-IDD of the
103 GeoSoilEnviroConsortium (GSECARS) in the Advanced Photon Source (APS; Prakapenka et al.,
104 2008). X-ray energy was 30 keV. The X-ray diffraction images were collected using a Dectris

105 **Table 1: Experiment run table for in-situ X-ray diffraction experiments at high pressure (P) and**
 106 **temperature (T) conditions.**

Sample #	P (GPa)	T (K)	Phase assemblage	V_{FeO} (\AA^3)	V_{diamond} (\AA^3)
Sample #1 [†]	71-74(8)	1,700-1,900	Fe ₃ C, FeO, d,f-FeH, C	62.68(4)	
Sample #2	92(8)	2,000	Fe ₃ C, FeO, d,f-FeH, C	59.58(1)	
	117(8)	2,200	Fe ₃ C, FeO, d,f-FeH, C	56.42(0)	
	127(8)	2,000	Fe ₃ C, FeO, d-FeH, C	55.62(1)	
Sample #3 [‡]	120(8)	2,002	Fe ₃ C, FeO, d-FeH, C	55.96(1)	38.0(4)
	120(8)	1,998	Fe ₃ C, FeO, d-FeH, C	56.02(1)	38.0(4)
	125(13)	2,723	py, f-FeH, C, *		38.1(4)
	126(13)	2,758	py, f-FeH, C, *		38.0(4)
	133(13)	2,818	py, f-FeH, C, *		37.8(4)
	130(13)	2,970	py, f-FeH, C, *		38.0(4)
	131(13)	3,332	py, f-FeH, C, *		38.0(4)
	138(14)	3,862	py, f-FeH, C, *		37.9(4)
	140(14)	4,051	py, f-FeH, C, *		37.9(4)

107 **Pressure was calculated based on unit-cell volume (V) of FeO (B1) or diamond by using their equation of**
 108 **state parameters (Fischer et al., 2011; Dewaele et al., 2008). Temperature uncertainties are estimated to**
 109 **be <200 K. d-FeH: dhcp-FeH_x, C: diamond, f-FeH: fcc-FeH_x, py: pyrite-type FeO₂H_x. *: X-ray diffraction**
 110 **lines which can be assigned to either dhcp-FeH_x or tetragonal FeH₂. †Pressure and temperature were**
 111 **maintained in the ranges throughout the sample. ‡ Temperature was increased at the same spot over the**
 112 **runs.**

113
 114 Pilatus detector and analyzed using DIOPTAS (Clemens et al., 2015) and PeakPo (Shim et al.,
 115 2017). The exposure time was 5–10 seconds. Typical X-ray and laser beam diameters were ~5 and

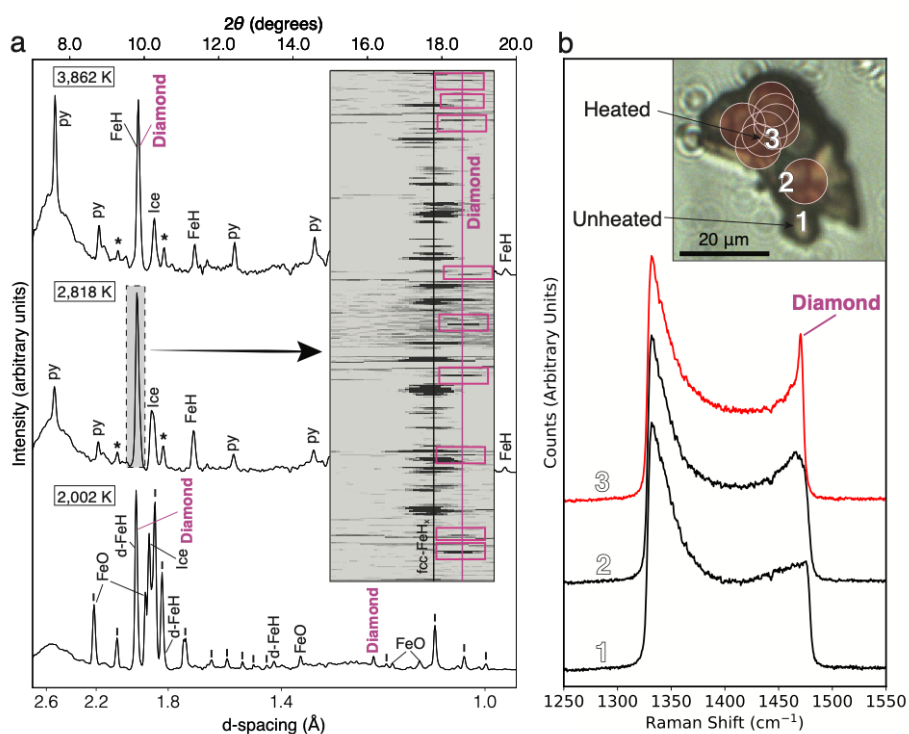
116 20 μm , respectively. The heating was conducted with a pre-set laser power which was directly
117 applied at the start of the heating and maintained for 5 seconds each heating cycle. This heating
118 method reduces the risk of overheating the diamond anvils particularly with water as a pressure
119 medium, preventing LHDACs from failure during high-temperature heating. For temperature
120 estimations, we fit the thermal radiation spectra measured from both sides of the sample to a Planck
121 gray-body equation for estimation of temperature. The temperature uncertainty is estimated to be
122 ~ 200 K considering the temperature reading difference between the two sides of the sample and
123 the intrinsic uncertainty from the spectroradiometry.

124 At relatively low temperatures ($< 2,200$ K), pressure was estimated using the equation of state
125 (EOS) parameters of FeO in NaCl-type structure (Fischer et al., 2011). At higher temperatures
126 ($> 2,700$ K) for Sample #3 (Table 1), reliable pressures were difficult to estimate, unlike at the
127 lower temperatures where robust diffraction lines of FeO are available. In this case, pressure was
128 estimated from the EOS of diamond (Dewaele et al., 2008) based on its 111 peak position, which
129 was identified more clearly than at lower temperatures. The calculations yield pressures up to
130 140 GPa (Table 1). The calculated pressures using the diamond at 2,000 K agree within 0.2–1.3%
131 with those estimated using the NaCl-type FeO in the same heating spot in Sample #3. Given the
132 fact that pressures of some runs are estimated from a single diffraction line, we assigned
133 conservative uncertainty (10%) for the pressures at temperatures over 2,700 K. The samples could
134 not be recovered to room conditions because of failure of diamond anvils during decompression
135 or sample loss when H_2O converts to liquid during decompression to ~ 1 bar.

136 Micro-Raman measurements were conducted for identifying diamond in Sample #1 at high
137 pressures. A solid-state (frequency doubled Nd:YAG) laser was used with a 532 nm
138 monochromatic beam at ASU. The laser power at the sample was ~ 3 mW. The spectrometer was
139 calibrated using the neon emission spectra. Measurements were conducted using an 1,800
140 grooves/mm grating. We calibrated pixel-to-pixel sensitivity differences in the charge-coupled
141 device (CCD) detector using the spectrum of a glass with well-known fluorescence intensities at
142 different wavenumbers. The exposure time for each spectrum measurement was 1–10 seconds.
143 Pressure was determined using a diamond anvil Raman gauge (Akahama and Kawamura, 2006).

144 3 Results

145 XRD peaks of Fe_3C and ice X were confirmed at high pressures before laser heating. The
 146 diffraction peaks were broad because of differential stress. After laser heating of the samples, we
 147 found two sets of mineral assemblages depending on heating temperature. At lower temperatures
 148 of 1,700–2,200 K at 71–127 GPa (Samples #1 and 2; Table 1), we observed the diffraction peaks
 149 of FeO (NaCl-type, B1), dhcp- FeH_x , and possibly diamond (Fig. 1a and S1). Some XRD patterns
 150 show fcc- FeH_x as an additional phase with relatively weak peak intensities (Table 1). The
 151 diffraction peaks of Fe_3C were also observed as sharp peaks. The characteristic diffraction line of
 152 diamond 111 was difficult to separate from that of dhcp- FeH_x 004. A run at 120 GPa and 2,002 K
 153 showed a clear diamond peak at $2\theta \sim 16^\circ$, which can be indexed as the 022 line (Fig. 1a).



154
 155 **Figure 1: (a) In-situ X-ray diffraction (XRD) patterns of the sample at 120–138 GPa and 2,002–**
 156 **3,862 K in laser-heated diamond anvil cell. X-ray energy was 30 keV. The background is subtracted.**
 157 **Py: pyrite-type FeOOH_x ; FeH: fcc- FeH_x ; Ice: Ice X; d-FeH: dhcp- FeH_x . The black vertical ticks**
 158 **represent Fe_3C . The asterisks indicate a minor iron hydride phase (dhcp- FeH_x or FeH_2). The inset**
 159 **displays a 2-D diffraction image corresponding to the peak in the grey box for 2θ angles of (horizontal**

160 axis) 9.5–10° and azimuth angles of 0–360° (vertical axis). The observed diamond 111 (the magenta
161 rectangles) is clearly distinguished from the fcc-FeH_x line. (b) High-pressure Raman spectra of the
162 sample at 54.9 GPa and 300 K. The sample was synthesized at 60 GPa and 2,000 K. The semi-
163 transparent red circles in the inset optical image represent heated areas. The locations of the
164 measured spectra are numbered in the inset. The sharp peak of the red spectrum at 1470 cm⁻¹ is from
165 diamond crystals formed by the reaction between Fe₃C and H₂O in the heated part of the sample.

166

167 We further examined the sample synthesized at ~72 GPa and ~1,800 K in Raman spectroscopy
168 (Sample #1; Table 1). In order to reduce the signal from the diamond anvils and enhance the signal
169 from diamond formed from the reaction in the sample, we used the confocal micro-Raman
170 technique which blocks out-of-focus light in signal detection. The strong peak at 1,320 cm⁻¹ is
171 from the uncompressed part of the diamond anvils (Fig. 1b). The right-hand side of the peak
172 extends up to 1,470 cm⁻¹, which is from the compressed part of the diamond anvils. Because the
173 diamond inside the sample is at a higher pressure than diamond anvil, the peak would appear at
174 the end of the spectral feature (~1,470 cm⁻¹). The heated areas clearly showed a sharp peak at the
175 edge of the spectral feature, whereas the unheated areas do not show such a peak (Fig. 1b),
176 demonstrating the existence of diamond formed from the reaction between Fe₃C and H₂O. Raman
177 spectra measured during decompression also showed the consistent results at 64, 55, 41, and 6 GPa
178 (Fig. S2). At a temperature range of 1,700-2,200 K, the reaction can be summarized as:

179



180 At higher temperatures of 2,700–4,050 K (Sample #3), we observed the formation of pyrite-type
181 FeOOH_x (py-FeOOH_x), fcc-FeH_x, and diamond at 125–140 GPa (Fig. 1a). The diffraction lines
182 of py-FeOOH_x and fcc-FeH_x are robustly observed. There are two unassigned diffraction peaks
183 with weak intensities (labeled with “*” in Fig. 1a), which can be indexed with either dhcp-FeH_x
184 or FeH₂ (Fig. 1a). In either case, it is likely that the thermal gradient during laser heating promoted
185 an appearance of additional iron hydride as a minor phase. At 3,860 K, the diffraction patterns
186 remain similar to those measured at 2,720 K (Fig. 1a), but with stronger intensity in general,
187 suggesting higher degree of reaction. The observation of diffraction lines for ice X is likely due to
188 the axial thermal gradients as H₂O should be molten if excess H₂O exists (Schwager et al., 2004).
189 Similarly, we infer that the diffraction lines of py-FeOOH_x came from the cooler sample regions

190 along the axial thermal gradients because its dehydration temperature is lower (Nishi et al., 2017)
191 than the heating temperatures. We observed diffuse scattering in the diffraction patterns at
192 temperatures over 2,700 K (Fig. S3) caused by melting. Temperatures greater than 2,700 K at 120–
193 140 GPa are higher than the reported solidus of Fe_3C (Mashino et al. 2019), as well as the
194 extrapolated solidus of FeH_x (Sakamaki et al., 2009). Therefore, the metallic melt should be rich
195 in H at the heating center. Diamond should be stable under the studied P – T conditions because of
196 its extremely high melting temperature ($\sim 7,000$ K at 130 GPa; Wang et al., 2005) as observed in
197 both XRD patterns and Raman spectra.

198 **4 Discussion**

199 4.1 Chemical Exchange Between the Mantle and Core

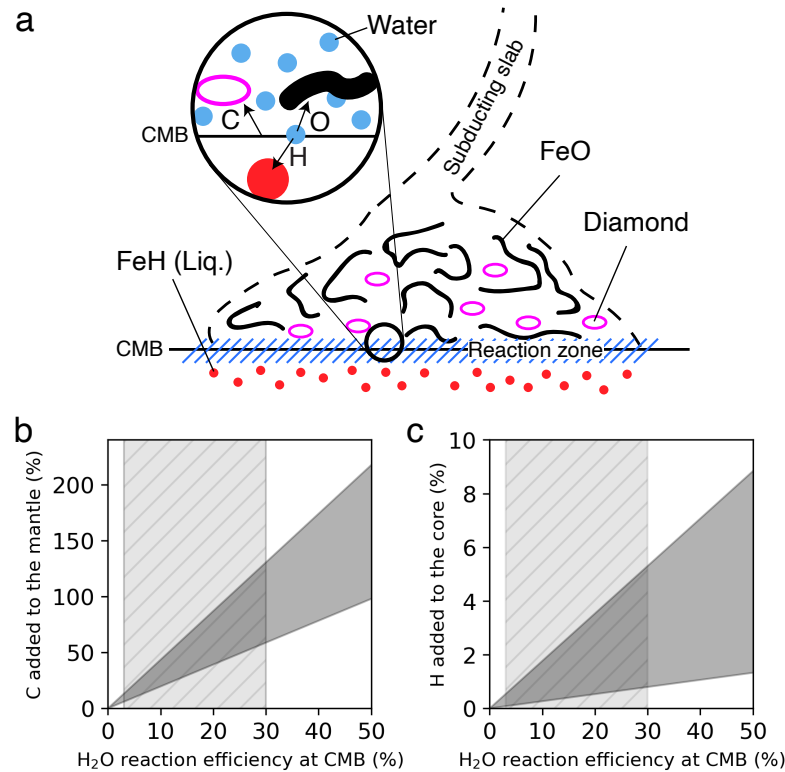
200 Previous experiments of paraffin + Fe metal showed that H is more siderophile than C, forming
201 diamond at lower-mantle conditions (Narygina et al., 2011; Hirose et al., 2019), although it
202 remains unclear that the reduced hydrogen can be provided to the lower mantle (Hu et al., 2016;
203 Nishi et al., 2017). In our experiments of $\text{Fe}_3\text{C} + \text{H}_2\text{O}$, similar partitioning behaviors of H and C
204 resulted in the formation of diamond. The formation of FeO and FeH_x observed in our experiments
205 with excess water is consistent with previous experiments of $2\text{Fe} + \text{H}_2\text{O} = \text{FeO} + 2\text{FeH}$ with less
206 water (6 wt% H_2O) at similar pressures and temperatures (~ 120 GPa and 2,000–2,250 K; Nishi et
207 al., 2020). Also, the decomposition of H_2O at the CMB shown in this study agrees well with other
208 experiments (Mao et al., 2017; Yuan et al., 2018).

209 This study demonstrates that not only water can play a critical role in chemical exchange between
210 the mantle and the core, but also Earth's carbon cycle is closely linked to the H and O cycles. Our
211 results found that at CMB conditions, metallic melt (rich in Fe and H) would form and most likely
212 be incorporated into the liquid outer core (Fig. 2a). Some amount of O would remain in the mantle
213 as iron oxide (FeO), while the metallic melt may also carry O to the core.

214 The water release from the dehydration of hydrous minerals in subducting slabs may have been a
215 continuous process from when the hydrated slabs first reached the CMB following the initiation
216 of plate tectonics. Although the timing of the onset of subduction is not well constrained, studies
217 indicate that subduction might have initiated 2.5–3.5 Ga (Laurent et al., 2014; Tang et al., 2016;

218 Condie and Kröner, 2008). Theoretical and experimental studies have suggested that subducting
 219 slabs would have been negatively buoyant in the transition zone and the topmost lower mantle
 220 since subduction initiated, thus promoting their descent to the deep lower mantle (Klein et al.,
 221 2017; Ko et al., 2020). If water in subducting slabs has been transported to the CMB and released
 222 in the region for ~3 billion years, the core-mantle chemical exchange presented here may have
 223 occurred during the time.

224 The carbon transfer from the core to the mantle results in the gradual augmentation of the mantle
 225 carbon for a significant portion of the Earth's history. This is consistent with the earlier hypothesis
 226 that water may facilitate carbon transfer at the CMB by Dasgupta et al. (2013), which may



227

228 **Figure 2: (a) Schematic diagram of the core-mantle boundary (CMB) region. Water (blue droplets**
 229 **in the inset) released from dehydration of a subducted slab causes a chemical reaction with liquid**
 230 **iron core in a reaction zone (blue shade) at the CMB. Diamond (magenta circles) and FeO (black**
 231 **lines) could be incorporated into the mantle, while hydrogen (red dots) could alloy with iron metal in**
 232 **the outer core. (b) The amount of carbon extracted from the core to the mantle for 3 Ga relative to**
 233 **the carbon content in the present-day mantle (120 ppm C; Mcdonough and Sun, 1995). (c) The**

234 amount of hydrogen added to the core for 3 Ga relative to the hydrogen content in the present-day
235 outer core (0.3–2.0 wt%; Terasaki et al., 2012; Umemoto and Hirose, 2015; Thompson et al., 2018;
236 Tagawa et al., 2021). (b, c) H₂O reaction efficiency at the CMB represents the water amount reacting
237 with the core at the CMB divided by the water amount subducted at the surface (Cai et al., 2018; see
238 Supplementary information for detail). The hatched area represents the 3–30% of the reaction
239 efficiency.

240

241 account for the present-day mantle carbon content (e.g., 120 ppm C; McDonough and Sun, 1995).
242 However, the form of carbon produced from the CMB reaction in the present study is diamond,
243 different from the oxidized carbon assumed by Dasgupta et al.

244 The amount of core carbon added to the mantle by the water-induced reaction at the CMB (after
245 core formation) can be estimated. Efficiency of the reaction was defined as the water amount
246 participating in the reaction at the CMB divided by the water amount subducted at the Earth's
247 surface (see Supplementary information for detail). It should be noted that how much subducted
248 water reaches the CMB is poorly constrained because of large uncertainties in dehydration and re-
249 hydration processes in the mantle (Walter, 2021). In this estimation, a constant rate of water
250 transport was assumed via subduction from the surface (3×10^{12} kg/yr H₂O for the global water
251 flux at the surface in present day; Cai et al., 2018) for 3 Ga. Also, we assumed a constant carbon
252 content in the outer core (0.9–2.0 wt%; Nakajima et al., 2015; Li et al., 2019). If 3–30% of
253 subducted water reaches the CMB and reacts with the core (see Supplementary Information for
254 detail), 7–160 ppm C can be added to the mantle over 3 Ga after core formation.

255 The proposed model thus has the potential to account for a substantial portion of the present-day
256 carbon in the mantle. For example, 120 ppm of the present-day carbon content (McDonough and
257 Sun, 1995) can be explained solely by the water-induced carbon transfer from the core (Fig. 2b),
258 if water has been efficiently transported to the CMB over the last 3 Ga. Yet, this calculated “core
259 carbon extraction” is only 0.2–1.7% ($0.3\text{--}6.3 \times 10^{20}$ kg C) of the estimated carbon content of the
260 present-day outer core (Nakajima et al., 2015; Li et al., 2019). Therefore, most of the core carbon
261 incorporated during its formation would still remain there. In addition, the model can estimate the
262 amount of hydrogen added to the core through the water-induced reaction. If hydrogen alloys with
263 iron metal with a 1:1 molar ratio (Supplementary Information), for the above assumed water

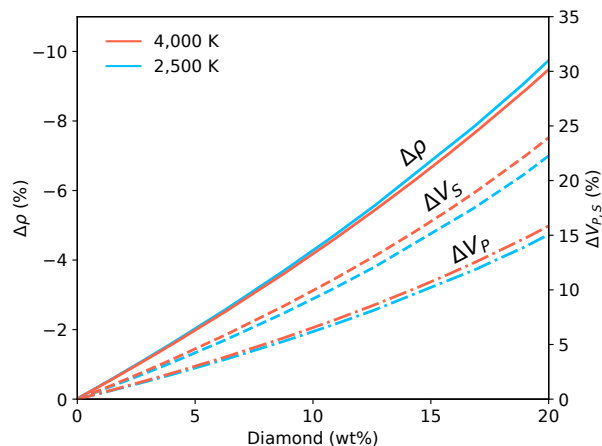
264 transport efficiency for the core carbon extraction, our calculation predicts that the amount of
265 hydrogen added to the outer core ($0.3\text{--}3.0 \times 10^{20}$ kg H) accounts for only 0.1–5.3% of the
266 estimated present-day core hydrogen (Terasaki et al., 2012; Umemoto and Hirose, 2015;
267 Thompson et al., 2018; Tagawa et al., 2021; Fig. 2c). Therefore, the core’s carbon and hydrogen
268 budgets would not be altered significantly by the core carbon extraction and are mainly determined
269 during core formation.

270 4.2 Seismic implications

271 Diamond formed at the CMB is expected to be advected by mantle flow, ultimately entrained by
272 upwelling mantle currents. This process is facilitated by the anomalously low density of diamond
273 (32% lower than the surrounding mantle). Therefore, diamond residency at the CMB may be
274 limited, but small-scale convection on the CMB may lead to temporary localized accumulations
275 of diamonds even in regions strongly affected by subducted slabs in the lowermost mantle
276 (Solomatov and Moresi, 2002; Li, 2020). Thus, regions with diamonds may not be ubiquitous at
277 the CMB, but we expect their presence in CMB regions of deeply subducting hydrated slabs.

278 A question pertains whether the lowermost mantle diamond can be advected by upwelling mantle
279 to the uppermost mantle. Diamond may react with metallic iron in the lower mantle to form iron
280 carbide during ascent, but diamond can coexist with Fe_7C_3 if the carbon proportion is over 8 wt%
281 (Lord et al., 2009). The upwelling flow would undergo an inevitable redox change when passing
282 the 660-km discontinuity where Fe^{3+} -rich bridgmanite is destabilized and diamond is oxidized to
283 carbonatite melts (Rohrbach and Schmidt, 2011). Such a redox change would make the upwelling
284 of the lowermost mantle diamond to the uppermost mantle difficult. However, the carbonatite melt
285 can still carry information about other minerals entrained together with the diamond from the
286 CMB. If the melt crystallizes new diamond that is sent to the surface, diamond inclusions can
287 exhibit geochemical signatures of their deep origin. Some diamond inclusions show low Mg# (0.2–
288 0.6) in magnesiowüstite (Harte and Hudson, 2013; Hayman, et al., 2005; Kaminsky et al., 2009;
289 Wirth et al., 2014) and an association of iron carbide and diamond (Kaminsky and Wirth, 2011),
290 suggesting the possibility of their deep origin at the CMB, as advocated in this study.

291



292
 293 **Figure 3: Density (solid lines), compressional (dotted-dashed lines), and shear wave velocities (dashed**
 294 **lines) of diamond + pyrolite with respect to pure pyrolite at the core-mantle boundary conditions**
 295 **(136 GPa). The red and blue lines were calculated for 4,000 and 2,500 K, respectively.**

296
 297 Diamond exhibits higher bulk and shear moduli as well as lower density compared to major mantle
 298 minerals (Valdez et al., 2012), and therefore 50–72% and 74–110% higher P (V_P) and S wave
 299 velocities (V_S), respectively, than pyrolite in the lower mantle. We calculated the V_S and density
 300 for the mineral assemblage of pyrolite + diamond with varying diamond proportion (0–20 wt%) at
 301 the CMB conditions (136 GPa and 2,500–4,000 K) using the `Perple_X` thermodynamic modeling
 302 program (Connolly, 2009) with the SBL2011 dataset (Stixrude and Lithgow-Bertelloni, 2011) and
 303 seismic properties of diamond (Dewaele et al., 2008; Valdez et al., 2012). The calculation
 304 demonstrates that even a small amount of diamond mixed with the background mantle can
 305 dramatically decrease density and increase V_P and V_S at the CMB (Fig. 3). Therefore, if diamond-
 306 bearing structures exist at the CMB, their exceptionally fast velocities could be detectable in
 307 seismic studies. Considering the fact that less dense structures could have longer resident time in
 308 regions with strong downgoing flow, the high velocity structures could be found regions associated
 309 with subducting slabs in the lowermost mantle.

310 5. Conclusions

311 We conducted experiments on reaction between Fe_3C and H_2O using LHDACs combined with in-
 312 situ X-ray diffraction at 70–140 GPa and up to 4,050 K. We found that the reaction liberates carbon

313 in the form of diamond as hydrogen and oxygen alloy with iron. This result implies that the Earth's
314 core carbon may have been transferred to the mantle if subducted water has reacted with the core.
315 Our model provides a testable prediction that such diamonds, if locally collected by mantle flow,
316 lead to small-scale high velocity structures near the subducted materials at the CMB.

317 **Acknowledgments**

318 This work has been supported by National Science Foundation (NSF) EAR-CSEDI-1401270 and
319 EAR-1921298 and the National Aeronautics and Space Administration (NASA) Exoplanet
320 80NSSC18K0353. B. Chen acknowledges the support from NSF grants EAR-1555388 and EAR-
321 2127807. This research used resources of the Advanced Photon Source (APS), a U.S. Department
322 of Energy (DOE) Office of Science User Facility operated for the DOE Office of Science by
323 Argonne National Laboratory under Contract No. DE-AC02-06CH11357. We acknowledge the
324 support of GeoSoilEnviroCARS (Sector 13), which is supported by the National Science
325 Foundation (NSF) - Earth Sciences (EAR-1634415), and the Department of Energy, Geosciences
326 (DE-FG02-94ER14466).

327 **Data Availability Statement**

328 Datasets for this research are available online (<https://doi.org/10.5281/zenodo.6040059>).

329 **References**

330 Akahama, Y., & Kawamura, H. (2006). Pressure calibration of diamond anvil Raman gauge to
331 310 GPa. *Journal of Applied Physics*, 100(4), 043516.

332 Cai, C., Wiens, D. A., Shen, W., & Eimer, M. (2018). Water input into the Mariana subduction
333 zone estimated from ocean-bottom seismic data. *Nature*, 563(7731), 389-392.

334 Condie, K. C., & Kröner, A. (2008). When did plate tectonics begin?: Evidence from the
335 geologic record. *Geological Society of America Special Papers*, 440, 281-294.

- 336 Connolly, J. A. D. (2009). The geodynamic equation of state: what and how. *Geochemistry,*
337 *Geophysics, Geosystems, 10*(10).
- 338 Dasgupta, R., & Walker, D. (2008). Carbon solubility in core melts in a shallow magma ocean
339 environment and distribution of carbon between the Earth's core and the mantle. *Geochimica et*
340 *Cosmochimica Acta, 72*(18), 4627-4641.
- 341 Dasgupta, R., Chi, H., Shimizu, N., Buono, A. S., & Walker, D. (2013). Carbon solution and
342 partitioning between metallic and silicate melts in a shallow magma ocean: Implications for the
343 origin and distribution of terrestrial carbon. *Geochimica et Cosmochimica Acta, 102*, 191-212.
- 344 Deines, P. (2002). The carbon isotope geochemistry of mantle xenoliths. *Earth-Science Reviews,*
345 *58*(3-4), 247-278.
- 346 Dewaele, A., Datchi, F., Loubeyre, P., & Mezouar, M. (2008). High pressure–high temperature
347 equations of state of neon and diamond. *Physical Review B, 77*(9), 094106.
- 348 Fischer, R. A., Campbell, A. J., Shofner, G. A., Lord, O. T., Dera, P., & Prakapenka, V. B.
349 (2011). Equation of state and phase diagram of FeO. *Earth and Planetary Science Letters, 304*(3-
350 4), 496-502.
- 351 Fischer, R. A., Cottrell, E., Hauri, E., Lee, K. K., & Le Voyer, M. (2020). The carbon content of
352 Earth and its core. *Proceedings of the National Academy of Sciences, 117*(16), 8743-8749.
- 353 Harte, B. (2010). Diamond formation in the deep mantle: the record of mineral inclusions and
354 their distribution in relation to mantle dehydration zones. *Mineralogical Magazine, 74*(2), 189-
355 215.

- 356 Harte, B., & Hudson, N. F. (2013). Mineral associations in diamonds from the lowermost upper
357 mantle and uppermost lower mantle. In *Proceedings of 10th International Kimberlite*
358 *Conference*, New Delhi (pp. 235-253). Springer.
- 359 Hayman, P. C., Kopylova, M. G., & Kaminsky, F. V. (2005). Lower mantle diamonds from Rio
360 Soriso (Juina area, Mato Grosso, Brazil). *Contributions to Mineralogy and Petrology*, 149(4),
361 430-445.
- 362 Hirose, K., Labrosse, S., & Hernlund, J. (2013). Composition and state of the core. *Annual*
363 *Review of Earth and Planetary Sciences*, 41, 657-691.
- 364 Hirose, K., Tagawa, S., Kuwayama, Y., Sinmyo, R., Morard, G., Ohishi, Y., & Genda, H.
365 (2019). Hydrogen limits carbon in liquid iron. *Geophysical Research Letters*, 46(10), 5190-5197.
- 366 Hirschmann, M. M., & Dasgupta, R. (2009). The H/C ratios of Earth's near-surface and deep
367 reservoirs, and consequences for deep Earth volatile cycles. *Chemical Geology*, 262(1-2), 4-16.
- 368 Hu, Q., Kim, D. Y., Yang, W., Yang, L., Meng, Y., Zhang, L., & Mao, H. K. (2016). FeO₂ and
369 FeOOH under deep lower-mantle conditions and Earth's oxygen-hydrogen
370 cycles. *Nature*, 534(7606), 241-244.
- 371 Kaminsky, F. V., Khachatryan, G. K., Andreazza, P., Araujo, D., & Griffin, W. L. (2009). Super-
372 deep diamonds from kimberlites in the Juina area, Mato Grosso State, Brazil. *Lithos*, 112, 833-
373 842.
- 374 Kaminsky, F. V., & Wirth, R. (2011). Iron carbide inclusions in lower-mantle diamond from
375 Juina, Brazil. *The Canadian Mineralogist*, 49(2), 555-572.
- 376 Kaminsky, F. (2012). Mineralogy of the lower mantle: A review of 'super-deep' mineral
377 inclusions in diamond. *Earth-Science Reviews*, 110(1-4), 127-147.

378 Kerridge, J. F. (1985). Carbon, hydrogen and nitrogen in carbonaceous chondrites: Abundances
379 and isotopic compositions in bulk samples. *Geochimica et Cosmochimica Acta*, 49(8), 1707-
380 1714.

381 Klein, B. Z., Jagoutz, O., & Behn, M. D. (2017). Archean crustal compositions promote full
382 mantle convection. *Earth and Planetary Science Letters*, 474, 516-526.

383 Ko, B., Prakapenka, V., Kunz, M., Prescher, C., Leinenweber, K., & Shim, S. H. (2020).
384 Mineralogy and density of Archean volcanic crust in the mantle transition zone. *Physics of the*
385 *Earth and Planetary Interiors*, 305, 106490.

386 Laurent, O., Martin, H., Moyen, J. F., & Doucelance, R. (2014). The diversity and evolution of
387 late-Archean granitoids: Evidence for the onset of “modern-style” plate tectonics between 3.0
388 and 2.5 Ga. *Lithos*, 205, 208-235.

389 Li, M. (2020). The formation of hot thermal anomalies in cold subduction-influenced regions of
390 Earth's lowermost mantle. *Journal of Geophysical Research: Solid Earth*, 125(6),
391 e2019JB019312.

392 Li, Y., Vočadlo, L., Alfè, D., & Brodholt, J. (2019). Carbon partitioning between the Earth's
393 inner and outer core. *Journal of Geophysical Research: Solid Earth*, 124(12), 12812-12824.

394 Lin, Y., Hu, Q., Meng, Y., Walter, M., & Mao, H. K. (2020). Evidence for the stability of
395 ultrahydrous stishovite in Earth's lower mantle. *Proceedings of the National Academy of*
396 *Sciences*, 117(1), 184-189.

397 Lord, O. T., Walter, M. J., Dasgupta, R., Walker, D., & Clark, S. M. (2009). Melting in the Fe-C
398 system to 70 GPa. *Earth and Planetary Science Letters*, 284(1-2), 157-167.

399 Mao, H. K., Hu, Q., Yang, L., Liu, J., Kim, D. Y., Meng, Y., ... & Mao, W. L. (2017). When
400 water meets iron at Earth's core–mantle boundary. *National Science Review*, 4(6), 870-878.

401 Mashino, I., Miozzi, F., Hirose, K., Morard, G., & Sinmyo, R. (2019). Melting experiments on
402 the Fe–C binary system up to 255 GPa: Constraints on the carbon content in the Earth's
403 core. *Earth and Planetary Science Letters*, 515, 135-144.

404 McDonough, W. F., & Sun, S. S. (1995). The composition of the Earth. *Chemical*
405 *geology*, 120(3-4), 223-253.

406 McDonough, W. F. (2003). 3.16–Compositional model for the Earth's core. *Treatise on*
407 *geochemistry*, 2, 547-568.

408 Nakajima, Y., Imada, S., Hirose, K., Komabayashi, T., Ozawa, H., Tateno, S., ... & Baron, A. Q.
409 (2015). Carbon-depleted outer core revealed by sound velocity measurements of liquid iron–
410 carbon alloy. *Nature communications*, 6(1), 1-7.

411 Narygina, O., Dubrovinsky, L. S., McCammon, C. A., Kurnosov, A., Kantor, I. Y., Prakapenka,
412 V. B., & Dubrovinskaia, N. A. (2011). X-ray diffraction and Mössbauer spectroscopy study of
413 fcc iron hydride FeH at high pressures and implications for the composition of the Earth's
414 core. *Earth and Planetary Science Letters*, 307(3-4), 409-414.

415 Nishi, M., Irifune, T., Tsuchiya, J., Tange, Y., Nishihara, Y., Fujino, K., & Higo, Y. (2014).
416 Stability of hydrous silicate at high pressures and water transport to the deep lower
417 mantle. *Nature Geoscience*, 7(3), 224-227.

418 Nishi, M., Kuwayama, Y., Tsuchiya, J., & Tsuchiya, T. (2017). The pyrite-type high-pressure
419 form of FeOOH. *Nature*, 547(7662), 205-208.

420 Nishi, M., Kuwayama, Y., Hatakeyama, T., Kawaguchi, S., Hirao, N., Ohishi, Y., & Irifune, T.
421 (2020). Chemical Reaction Between Metallic Iron and a Limited Water Supply Under Pressure:
422 Implications for Water Behavior at the Core-Mantle Boundary. *Geophysical Research*
423 *Letters*, 47(19), e2020GL089616.

424 Nisr, C., Chen, H., Leinenweber, K., Chizmeshya, A., Prakapenka, V. B., Prescher, C., ... &
425 Shim, S. H. (2020). Large H₂O solubility in dense silica and its implications for the interiors of
426 water-rich planets. *Proceedings of the National Academy of Sciences*, 117(18), 9747-9754.

427 Núñez Valdez, M., Umemoto, K., & Wentzcovitch, R. M. (2012). Elasticity of diamond at high
428 pressures and temperatures. *Applied Physics Letters*, 101(17), 171902.

429 Piet, H., Leinenweber, K. D., Tappan, J., Greenberg, E., Prakapenka, V. B., Buseck, P. R., &
430 Shim, S. H. (2020). Dehydration of δ -AlOOH in Earth's Deep Lower Mantle. *Minerals*, 10(4),
431 384.

432 Prakapenka, V. B., Kubo, A., Kuznetsov, A., Laskin, A., Shkurikhin, O., Dera, P., ... & Sutton,
433 S. R. (2008). Advanced flat top laser heating system for high pressure research at GSECARS:
434 application to the melting behavior of germanium. *High Pressure Research*, 28(3), 225-235.

435 Prescher, C., & Prakapenka, V. B. (2015). DIOPTAS: a program for reduction of two-
436 dimensional X-ray diffraction data and data exploration. *High Pressure Research*, 35(3), 223-
437 230.

438 Rohrbach, A., & Schmidt, M. W. (2011). Redox freezing and melting in the Earth's deep mantle
439 resulting from carbon-iron redox coupling. *Nature*, 472(7342), 209-212.

440 Sakamaki, K., Takahashi, E., Nakajima, Y., Nishihara, Y., Funakoshi, K., Suzuki, T., & Fukai,
441 Y. (2009). Melting phase relation of FeH_x up to 20 GPa: Implication for the temperature of the
442 Earth's core. *Physics of the Earth and Planetary Interiors*, 174(1-4), 192-201.

- 443 Schwager, B., Chudinovskikh, L., Gavriiliuk, A., & Boehler, R. (2004). Melting curve of H₂O to
444 90 GPa measured in a laser-heated diamond cell. *Journal of Physics: Condensed Matter*, *16*(14),
445 S1177.
- 446 Shim, S. H. (2017). PeakPo - A python software for X-ray diffraction analysis at high pressure
447 and high temperature. *Zenodo*. <http://doi.org/10.5281/zenodo.810199>
- 448 Solomatov, V. S., & Moresi, L. N. (2002). Small-scale convection in the D'' layer. *Journal of*
449 *Geophysical Research: Solid Earth*, *107*(B1), ETG-3.
- 450 Stixrude, L., & Lithgow-Bertelloni, C. (2011). Thermodynamics of mantle minerals-II. Phase
451 equilibria. *Geophysical Journal International*, *184*(3), 1180-1213.
- 452 Tagawa, S., Sakamoto, N., Hirose, K., Yokoo, S., Hernlund, J., Ohishi, Y., & Yurimoto, H.
453 (2021). Experimental evidence for hydrogen incorporation into Earth's core. *Nature*
454 *communications*, *12*(1), 1-8.
- 455 Tang, M., Chen, K., & Rudnick, R. L. (2016). Archean upper crust transition from mafic to felsic
456 marks the onset of plate tectonics. *Science*, *351*(6271), 372-375.
- 457 Terasaki, H., Ohtani, E., Sakai, T., Kamada, S., Asanuma, H., Shibazaki, Y., ... & Funakoshi, K.
458 I. (2012). Stability of Fe–Ni hydride after the reaction between Fe–Ni alloy and hydrous phase
459 (δ -AlOOH) up to 1.2 Mbar: Possibility of H contribution to the core density deficit. *Physics of*
460 *the Earth and Planetary Interiors*, *194*, 18-24.
- 461 Thompson, E. C., Davis, A. H., Bi, W., Zhao, J., Alp, E. E., Zhang, D., ... & Campbell, A. J.
462 (2018). High-pressure geophysical properties of Fcc phase FeH_x. *Geochemistry, Geophysics,*
463 *Geosystems*, *19*(1), 305-314.

464 Umemoto, K., & Hirose, K. (2015). Liquid iron-hydrogen alloys at outer core conditions by first-
465 principles calculations. *Geophysical Research Letters*, 42(18), 7513-7520.

466 Walter, M. J. (2021). Water transport to the core–mantle boundary. *National Science*
467 *Review*, 8(4), nwab007.

468 Wang, X., Scandolo, S., & Car, R. (2005). Carbon phase diagram from ab initio molecular
469 dynamics. *Physical review letters*, 95(18), 185701.

470 Wänke, H. (1981). Constitution of terrestrial planets. *Philosophical Transactions of the Royal*
471 *Society of London. Series A, Mathematical and Physical Sciences*, 303(1477), 287-302.

472 Wirth, R., Dobrzhinetskaya, L., Harte, B., Schreiber, A., & Green, H. W. (2014). High-Fe
473 (Mg,Fe)O inclusion in diamond apparently from the lowermost mantle. *Earth and Planetary*
474 *Science Letters*, 404, 365-375.

475 Wood, B. J., Li, J., & Shahar, A. (2013). Carbon in the core: its influence on the properties of
476 core and mantle. *Reviews in Mineralogy and Geochemistry*, 75(1), 231-250.

477 Yu, S., & Garnero, E. J. (2018). Ultralow velocity zone locations: A global
478 assessment. *Geochemistry, Geophysics, Geosystems*, 19(2), 396-414.

479 Yuan, L., Ohtani, E., Ikuta, D., Kamada, S., Tsuchiya, J., Naohisa, H., ... & Suzuki, A. (2018).
480 Chemical reactions between Fe and H₂O up to megabar pressures and implications for water
481 storage in the Earth's mantle and core. *Geophysical Research Letters*, 45(3), 1330-1338.

482 **References From the Supporting Information**

483 Fei, H., & Katsura, T. (2020). High water solubility of ringwoodite at mantle transition zone
484 temperature. *Earth and Planetary Science Letters*, 531, 115987.

- 485 Fu, S., Yang, J., Karato, S. I., Vasiliev, A., Presniakov, M. Y., Gavriiliuk, A. G., ... & Lin, J. F.
486 (2019). Water concentration in single-crystal (Al, Fe)-bearing bridgmanite grown from the
487 hydrous melt: Implications for dehydration melting at the topmost lower mantle. *Geophysical*
488 *Research Letters*, 46(17-18), 10346-10357.
- 489 Iwamori, H. (2004). Phase relations of peridotites under H₂O-saturated conditions and ability of
490 subducting plates for transportation of H₂O. *Earth and Planetary Science Letters*, 227(1-2), 57-
491 71.
- 492 van Keken, P. E., Hacker, B. R., Syracuse, E. M., & Abers, G. A. (2011). Subduction factory: 4.
493 Depth-dependent flux of H₂O from subducting slabs worldwide. *Journal of Geophysical*
494 *Research: Solid Earth*, 116(B1).
- 495 Okamoto, K., & Maruyama, S. (2004). The eclogite–garnetite transformation in the MORB+
496 H₂O system. *Physics of the Earth and Planetary Interiors*, 146(1-2), 283-296.
- 497 Shieh, S. R., Mao, H. K., Hemley, R. J., & Ming, L. C. (1998). Decomposition of phase D in the
498 lower mantle and the fate of dense hydrous silicates in subducting slabs. *Earth and Planetary*
499 *Science Letters*, 159(1-2), 13-23.